A Measurement of the ψ' to J/ψ Production Ratio in 920 GeV Proton-Nucleus Interactions

I. Abt[23], M. Adams[10], M. Agari[13], H. Albrecht[12], A. Aleksandrov[29], V. Amaral[8], A. Amorim[8], S. J. Aplin[12], V. Aushev[16], Y. Bagaturia[12,36], V. Balagura[22], M. Bargiotti[6], O. Barsukova[11], J. Bastos[8], J. Batista[8], C. Bauer[13], Th. S. Bauer[1], A. Belkov[11,†], Ar. Belkov[11], I. Belotelov[11], A. Bertin[6], B. Bobchenko[22], M. Böcker[26], A. Bogatyrev[22], G. Bohm[29], M. Bräuer[13], M. Bruinsma[28,1], M. Bruschi[6], P. Buchholz[26], T. Buran[24], J. Carvalho[8], P. Conde[2,12], C. Cruse[10], M. Dam[9], K. M. Danielsen[24], M. Danilov[22], S. De Castro[6], H. Deppe[14], X. Dong[3], H. B. Dreis[14], V. Egorytchev[12], K. Ehret[10], F. Eisele[14], D. Emeliyanov[12], S. Essenov[22], L. Fabbri[6], P. Faccioli[6], M. Feuerstack-Raible[14], J. Flammer[12], B. Fominykh[22], M. Funcke[10], Ll. Garrido[2], A. Gellrich[29], B. Giacobbe[6], J. Gläß[20], D. Goloubkov[12,33], Y. Golubkov[12,34], A. Golutvin[22], I. Golutvin[11], I. Gorbounov[12,26], A. Gorišek[17], O. Gouchtchine[22], D. C. Goulart[7], S. Gradl[14], W. Gradl[14], F. Grimaldi[6], J. Groth-Jensen[9], Yu. Guilitsky[22,35], J. D. Hansen[9], J. M. Hernández[29], W. Hofmann[13], M. Hohlmann[12], T. Hott[14], W. Hulsbergen[1], U. Husemann[26], O. Igonkina[22], M. Ispiryan[15], T. Jagla[13], C. Jiang[3], H. Kapitza[12], S. Karabekyan[25], N. Karpenko[11], S. Keller[26], J. Kessler[14], F. Khasanov[22], Yu. Kiryushin[11], I. Kisel[23], E. Klinkby[9], K. T. Knöpfle[13], H. Kolanoski[5], S. Korpar[21,17], C. Krauss[14], P. Kreuzer[12,19], P. Križan[18,17], D. Krücker[5], S. Kupper[17], T. Kvaratskheliia[22], A. Lanyov[11], K. Lau[15], B. Lewendel[12], T. Lohse[5], B. Lomonosov[12,32], R. Männer[20], R. Mankel[29], S. Masciocchi[12], I. Massa[6], I. Matchikhilian[22], G. Medin[5], M. Medinnis[12], M. Mevius[12], A. Michetti[12], Yu. Mikhailov[22,35], R. Mizuk[22], R. Muresan[9], M. zur Nedden[5], M. Negodaev[12,32], M. Nörenberg[12], S. Nowak[29], M. T. Núñez Pardo de Vera[12], M. Ouchrif[28,1], F. Ould-Saada[24], C. Padilla[12], D. Peralta[2], R. Pernack[25], R. Pestotnik[17], B. AA. Petersen[9], M. Piccinini[6], M. A. Pleier[13], M. Poli[6,31], V. Popov[22], D. Pose[11,14], S. Prystupa[16], V. Pugatch[16], Y. Pylypchenko[24], J. Pyrlik[15], K. Reeves[13], D. Reßing[12], H. Rick[14], I. Riu[12], P. Robmann[30], I. Rostovtseva[22], V. Rybnikov[12], F. Sánchez[13], A. Sbrizzi[1], M. Schmelling[13], B. Schmidt[12], A. Schreiner[29], H. Schröder[25], U. Schwanke[29], A. J. Schwartz[7], A. S. Schwarz[12], B. Schwenninger[10], B. Schwingenheuer[13], F. Sciacca[13], N. Semprini-Cesari[6], S. Shuvalov[22,5], L. Silva[8], L. Sözüer[12], S. Solunin[11], A. Somov[12], S. Somov[12,33], J. Spengler[12], R. Spighi[6], A. Spiridonov[29,22], A. Stanovnik[18,17], M. Starič[17], C. Stegmann[5], H. S. Subramania[15], M. Symalla[12,10], I. Tikhomirov[22], M. Titov[22], I. Tsakov[27], U. Uwer[14], C. van Eldik[12,10], Yu. Vassiliev[16], M. Villa[6], A. Vitale[6], I. Vukotic[5,29], H. Wahlberg[28], A. H. Walenta[26], M. Walter[29], J. J. Wang[4], D. Wegener[10], U. Werthenbach[26], H. Wolters[8], R. Wurth[12], A. Wurz[20], Yu. Zaitsev[22], M. Zavertyaev[12,13,32], T. Zeuner[12,26], A. Zhelezov[22], Z. Zheng[3], R. Zimmermann[25], T. Živko[17], and A. Zoccoli[6]

[1] *NIKHEF, 1009 DB Amsterdam, The Netherlands* [a]
[2] *Department ECM, Faculty of Physics, University of Barcelona, E-08028 Barcelona, Spain* [b]
[3] *Institute for High Energy Physics, Beijing 100039, P.R. China*
[4] *Institute of Engineering Physics, Tsinghua University, Beijing 100084, P.R. China*
[5] *Institut für Physik, Humboldt-Universität zu Berlin, D-12489 Berlin, Germany* [c,d]
[6] *Dipartimento di Fisica dell' Università di Bologna and INFN Sezione di Bologna, I-40126 Bologna, Italy*
[7] *Department of Physics, University of Cincinnati, Cincinnati, Ohio 45221, USA* [e]
[8] *LIP Coimbra, P-3004-516 Coimbra, Portugal* [f]
[9] *Niels Bohr Institutet, DK 2100 Copenhagen, Denmark* [g]
[10] *Institut für Physik, Universität Dortmund, D-44221 Dortmund, Germany* [d]

2

[11] *Joint Institute for Nuclear Research Dubna, 141980 Dubna, Moscow region, Russia*
[12] *DESY, D-22603 Hamburg, Germany*
[13] *Max-Planck-Institut für Kernphysik, D-69117 Heidelberg, Germany* [d]
[14] *Physikalisches Institut, Universität Heidelberg, D-69120 Heidelberg, Germany* [d]
[15] *Department of Physics, University of Houston, Houston, TX 77204, USA* [e]
[16] *Institute for Nuclear Research, Ukrainian Academy of Science, 03680 Kiev, Ukraine* [h]
[17] *J. Stefan Institute, 1001 Ljubljana, Slovenia* [i]
[18] *University of Ljubljana, 1001 Ljubljana, Slovenia*
[19] *University of California, Los Angeles, CA 90024, USA* [j]
[20] *Lehrstuhl für Informatik V, Universität Mannheim, D-68131 Mannheim, Germany*
[21] *University of Maribor, 2000 Maribor, Slovenia*
[22] *Institute of Theoretical and Experimental Physics, 117259 Moscow, Russia* [k]
[23] *Max-Planck-Institut für Physik, Werner-Heisenberg-Institut, D-80805 München, Germany* [d]
[24] *Dept. of Physics, University of Oslo, N-0316 Oslo, Norway* [l]
[25] *Fachbereich Physik, Universität Rostock, D-18051 Rostock, Germany* [d]
[26] *Fachbereich Physik, Universität Siegen, D-57068 Siegen, Germany* [d]
[27] *Institute for Nuclear Research, INRNE-BAS, Sofia, Bulgaria*
[28] *Universiteit Utrecht/NIKHEF, 3584 CB Utrecht, The Netherlands* [a]
[29] *DESY, D-15738 Zeuthen, Germany*
[30] *Physik-Institut, Universität Zürich, CH-8057 Zürich, Switzerland* [m]
[31] *visitor from Dipartimento di Energetica dell' Università di Firenze and INFN Sezione di Bologna, Italy*
[32] *visitor from P.N. Lebedev Physical Institute, 117924 Moscow B-333, Russia*
[33] *visitor from Moscow Physical Engineering Institute, 115409 Moscow, Russia*
[34] *visitor from Moscow State University, 119899 Moscow, Russia*
[35] *visitor from Institute for High Energy Physics, Protvino, Russia*
[36] *visitor from High Energy Physics Institute, 380086 Tbilisi, Georgia*
[†] *deceased*

Abstract Ratios of the ψ' over the J/ψ production cross sections in the dilepton channel for C, Ti and W targets have been measured in $920\,\mathrm{GeV}$ proton-nucleus interactions with the HERA-B detector at the HERA storage ring. The ψ' and J/ψ states were reconstructed in both the $\mu^+\mu^-$ and the e^+e^- decay modes. The measurements covered the kinematic range $-0.35 \le x_F \le 0.1$ with transverse momentum $p_T \le 4.5\,\mathrm{GeV}/c$. The ψ' to J/ψ production ratio is almost constant in the covered x_F range and shows a slow increase with p_T. The angular dependence of the ratio has been used to measure the difference of the ψ' and J/ψ polarization. All results for the muon and electron decay channels are in good agreement: their ratio, averaged over all events, is $R_{\psi'}(\mu)/R_{\psi'}(e) = 1.00 \pm 0.08 \pm 0.04$. This result constitutes a new, direct experimental constraint on the double ratio of branching fractions, $\left(B'(\mu) \cdot B(e)\right) / \left(B(\mu) \cdot B'(e)\right)$, of ψ' and J/ψ in the two channels.

1 Introduction

The hadroproduction of charmonium can be described by models [1–4] which rely on measured structure functions to describe partons in the initial state, perturbative QCD to calculate the production of intermediate $c\bar{c}$ states, and a subsequent non-perturbative hadronization step. Depending on the model assumptions and scope, this latter step must account for several effects, including color neutralization by soft gluon emission, bound state formation and the influence of nuclear matter ("nuclear suppression"). This in turn leads to the introduction of free parameters which are tuned to describe existing data. The tuned model can then be used to predict the production of charmonium states not considered in the tuning step or in other kinematic regimes.

Production of the ψ' in proton induced collisions has been measured over a wide range of energies in several experiments at Fermilab and CERN. But the experimental situation is still not satisfactory since most measurements suffer either from limited sample size or from additional large uncertainties resulting from signal extraction in the presence of large backgrounds. In many of the fixed-target experiments, absorber material was placed behind the target to reduce the muon background produced by pion and kaon decays in flight. For such experiments the e^+e^- mode was not observable and also the mass resolution suffered from the scattering of the muons in the absorber. In some cases, the mass resolution was insufficient for a separation of the J/ψ and ψ' signals.

In contrast, using the HERA-B detector's advanced particle identification and tracking systems, it was possible to reduce the background from π and K decays in flight by using track quality criteria without inserting absorber material, and thereby to have good mass resolution and also afford the possibility of triggering on and reconstructing electrons. The $\mu^+\mu^-$ and e^+e^- decay channels were recorded simultaneously. The rather large HERA-B samples of J/ψ and ψ' (300,000 and 5000 events , respectively) and well separated J/ψ and ψ' signals will contribute to the clarification of the experimental situation.

In order to minimize possible systematic biases introduced by acceptance and efficiency corrections, we report the ratio of the ψ' and J/ψ production cross section times the dilepton branching ratio. The sample size allows measurements of this ratio in several bins of the Feynman variable, x_F, and transverse momentum, p_T. The decay angular distribution of the ratio, which is related to the difference of the ψ' and J/ψ polarization was also studied.

The branching ratio of ψ' in the dimuon decay channel is not well known. The PDG value of the branching ratio $B'(\mu) = (0.73 \pm 0.08)\%$ [5] for ψ' has a relative error of 11% and is a factor of 3 less accurate than the corresponding branching ratio for the e^+e^- decay, $B'(e)$. Furthermore almost all measurements of ψ' to J/ψ production ratio have been performed in the $\mu^+\mu^-$ channel only. The production ratio measured in pp collisions by detecting e^+e^- pairs [6] is

Correspondence to: Alexander.Spiridonov@desy.de

rather imprecise (0.019 ± 0.007). Our relatively large samples in both channels therefore permit a sensitive test of $e - \mu$ universality in ψ' dilepton decays.

The paper is structured as follows. After a short description of the HERA-B detector, the trigger and the data sample in Sect. 2, the method used for the measurement of the ψ' and J/ψ production ratio is introduced in Sect. 3. The Monte Carlo simulation and the event reconstruction and selection are presented in Sects. 4 and 5. In Sect. 6, the difference of ψ' and J/ψ polarization is studied, followed by a discussion of sources of systematic uncertainties in Sect. 7. Finally, the experimental results are presented, the differential ψ' and J/ψ production ratio in Sect. 8, the inclusive ψ' and J/ψ production ratios in Sect. 9 and the nuclear dependence in Sect. 10. Sect. 11 confronts the HERA-B results with previous measurements and theoretical model predictions. The paper ends with conclusions given in Sect. 12.

2 Detector, trigger and data sample

The fixed target experiment HERA-B [7,8] was operated at the HERA storage ring at DESY until 2003. The forward spectrometer of HERA-B covered angles from 15 to 220 mrad in the bending plane and from 15 to 160 mrad vertically. The target [9] consisted of two independent stations, separated longitudinally by 4 cm along the beam. Each station contained four wires which could be independently positioned in the halo of the HERA proton beam (inner, outer, below and above with respect to the beam). Various materials (C, Ti, W) were used for the wires.

The tracking system consisted of the Vertex Detector System (VDS) followed by a magnetic dipole field of 2.13 Tm and a main tracker. The VDS [10] was a silicon strip detector with a pitch of $50\,\mu$m. The Inner Tracker (ITR) [11] of the main tracking system used micro-strip gas chambers with $300\,\mu$m pitch in the inner part of the main tracker up to distances of 25 cm around the proton beam. The Outer Tracker (OTR) [12,13] used honeycomb drift chambers with 5 and 10 mm diameter cells covering the remaining acceptance. A spatial resolution of about $150\,\mu$m and $360\,\mu$m was achieved for the ITR and OTR, respectively.

The main tracker system consisted of four stations immediately behind the magnet: the Pattern Chambers (PC), and two stations positioned further downstream: the Trigger Chambers (TC). A Ring Imaging Cherenkov detector (RICH) [14] was situated between the PC and TC stations. The TC chambers were mainly used by the trigger. The TC also served together with the PC to provide additional measurements of the track position and direction. The number of layers was 30 and 12 in the PC and TC chambers, respectively.

Particle identification was provided by the RICH, a MUON system and an Electromagnetic Calorimeter (ECAL). The ECAL [15] followed by the MUON system were located at the end of the spectrometer. The ECAL was optimized for good electron/gamma energy resolution and electron–hadron discrimination. The ECAL had variable granularity: the cell sizes were 2.2 cm, 5.5 cm and 11 cm in the inner, middle and outer part, respectively. The ECAL was instrumented with a fast digital read-out and a pretrigger system. The MUON system [16] consisted of four tracking stations at various depths in an iron or concrete absorber. Only muons above $5\,\mathrm{GeV}/c$ have a significant probability of penetrating through the absorbers.

The trigger chain included the ECAL and MUON pretrigger systems which provided lepton candidate seeds for the First Level Trigger (FLT) which in turn required at least two pretrigger seeds. Starting from the seeds, the FLT attempted to find tracks in a subset of the OTR tracking layers, requiring that at least one of the seeds results in a track. Starting once again from the pretrigger seeds, the Second Level Trigger (SLT) searched for tracks using all OTR layers and continued the tracking through the VDS, finally requiring at least two fully reconstructed tracks which were consistent with a common vertex hypothesis. The pretriggers and FLT are hardware

triggers which reduce with an output rate of typically 25 kHz while the SLT is a software trigger running on a farm of 240 Linux PCs.

This analysis is based on 164 million dilepton triggered events collected in the 2002–2003 physics runs. About 300,000 J/ψ lepton decays contained in the data sample are almost equally divided between the dimuon and dielectron channels. The wire materials used are carbon ($A = 12$, about 65% of the J/ψ data), tungsten ($A = 184$, about 31%) and titanium ($A = 48$, about 4%). Only runs in which detector components performed well and trigger conditions were stable were used. Six periods with constant experimental conditions are defined and the data are grouped accordingly.

3 Measurement method

The analysis is based on the selection of dilepton events and fitting of the dilepton invariant mass spectra in the area around the J/ψ and ψ' signals. The number of events in the J/ψ peak, N_ψ, is given by:

$$N_\psi = \sigma(J/\psi) \cdot B(J/\psi \to l^+l^-) \cdot \mathcal{L} \cdot \epsilon\,,$$

i.e. the product of the cross section ($\sigma(J/\psi)$), the branching ratio into dilepton pairs (B), the integrated luminosity ($\mathcal{L}$) and the total reconstruction efficiency (ϵ). The efficiency takes the following effects into account: the probability for leptons to be within the detector acceptance and to be properly registered in the detectors, the probability for the dilepton pair to be triggered, the probabilities to reconstruct the tracks and the dilepton vertex, and the probability to select the dileptons for the final analysis. The luminosity is identical for all charmonium states produced on the same targets, and therefore cancels in the ratios. The ratio of the ψ' and J/ψ cross sections in the l^+l^- channel, $R_{\psi'}(l)$, is equal to:

$$R_{\psi'}(l) = \frac{B' \cdot \sigma'}{B \cdot \sigma} = \frac{N_{\psi'}}{N_\psi} \cdot \frac{\epsilon}{\epsilon'}\,, \tag{1}$$

where l denotes the leptonic decay channel (e or μ), $\sigma(\sigma')$ is the J/ψ (ψ') production cross section and B (B') is the branching ratio for the l^+l^- decay of the J/ψ (ψ') meson.

The ratio $N_{\psi'}/N_\psi$ or "raw ψ'/ψ ratio", is defined from the fit of the J/ψ and ψ' signals and must be corrected by the efficiency ratio, ϵ/ϵ', where ϵ is defined above and ϵ' is the corresponding efficiency for detection of ψ' mesons. The efficiencies are evaluated by a Monte Carlo simulation.

For the analysis we select the kinematic domain

$$-0.35 < x_F < 0.10 \ \text{and} \ 0 < p_T < 4.5 \ \text{GeV}/c \tag{2}$$

for the Feynman variable x_F and the transverse momentum p_T, respectively. This domain corresponds to our acceptance range in x_F and at high p_T is limited by lack of ψ' events, i.e. is determined by the sample size.

4 Monte Carlo simulation

Results of Monte Carlo simulations (MC) were used to determine the efficiencies of J/ψ and ψ' triggering, reconstruction and selection. J/ψ and ψ' production was simulated by generating the basic process, $pN \to c\bar{c}X$ with PYTHIA 5.7 [17] and hadronizing the c and $\bar{c}$ quarks with JETSET 7.4 [17]. The momentum and energy of the remaining hadronic system, X, is given as input to FRITIOF 7.02 [18] which generates particles in the underlying event taking into account their interactions inside the nucleus.

The generated ψ' events were assigned weights such that the resulting weighted x_F distribution of the ψ' matched that of the J/ψ, since both measurements and theoretical models show little or no difference of these distributions in the kinematic domain Eq. (2) as described in Sect. 8. Additional weights were applied to both J/ψ and ψ' events such that the resulting p_T distribution matches

$$\frac{d\sigma}{dp_T^2} \propto \left[1 + \left(\frac{35\,\pi\,p_T}{256\,\langle p_T \rangle}\right)^2\right]^{-6}, \; \langle p_T \rangle = 1.29\,\text{GeV}/c. \tag{3}$$

The average transverse momentum, $\langle p_T \rangle$, in (3) was taken from a preliminary HERA-B analysis of the J/ψ sample [19]. The effects of possible differences in p_T and x_F distributions for the J/ψ and ψ' are described in Sect.7.

A GEANT 3.21 [20] based package [21] performed tracking of the particles through the HERA-B detector and the simulation of the detector response. The status (dead/alive), efficiency and noise level of each detector channel were inferred from the data separately for each of six running periods (see Sect. 2) and used in modeling the detector response. The MC events were reconstructed with the same code used for the data.

5 Event reconstruction and selection

The track reconstruction included the following steps: finding straight track segments in the VDS and PC area, propagation of the PC segments through the TC area, matching of VDS and PC segments and a full iterative fit of the tracks. The track segments were propagated into the TC area to provide a better measurement of the tracks in the RICH, ECAL and MUON detectors. Particle identification estimators were evaluated for each track using information from these three detectors.

Pairs of like sign and unlike sign candidates of muons and electrons were selected. A vertex fit was performed for each candidate with a weak cut on the χ^2 probability ($\geq 10^{-5}$) to ensure that the tracks originated from the same vertex. At this stage, 99% of the recorded J/ψ and ψ' candidates with reconstructed lepton tracks were selected. Further cuts and fits of the dilepton invariant mass spectra which were specific to the muon and electron modes will be discussed in the following two subsections.

5.1 Selection of J/ψ, $\psi' \rightarrow \mu^+\mu^-$

For the selection of $\mu^+\mu^-$ pairs, soft cuts were applied to the momenta ($400\,\text{GeV}/c > p > 6\,\text{GeV}/c$) and transverse momenta ($p_T > 0.7\,\text{GeV}/c$) of the muons. The lower cut values were close to the trigger requirements and the upper momentum cut rejected tracks outside the expected range for $J/\psi(\psi')$ decay products.

The main background in the muon channel was from muons produced in $K, \pi \rightarrow \mu\nu$ decays in flight. If a decay occurred inside the tracking system, the "broken trajectory" could have led to a large χ^2 in the track fit. A decay between the VDS and the PC could additionally have led to a poor match between VDS and PC track segments. The tracks from the main tracker were projected into the MUON system, where hits were associated with the track and used to obtain a χ^2–value with respect to the extrapolated track, taking into account multiple scattering. This muon–χ^2 was used to obtain a quality estimator varying from 0 to 1 and called the "muon likelihood". Kaon and pion decays between the PC and the MUON system could have led to a large muon–χ^2 and therefore a low muon likelihood, as could wrongly assigning MUON hits produced by another particle.
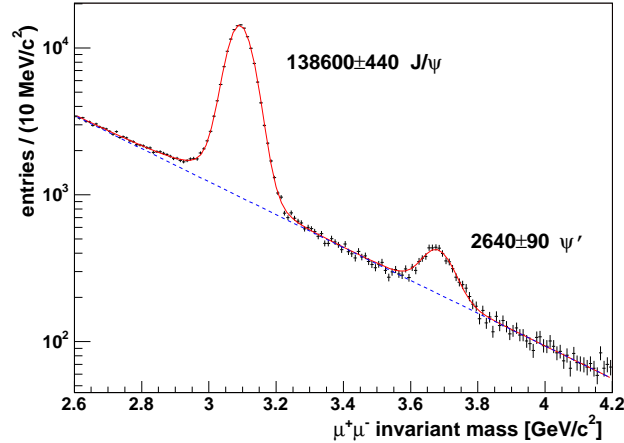
Figure 1. The invariant mass distribution of $\mu^+\mu^-$ in the region of the J/ψ and ψ' peaks for selected dimuons from all three targets and fitted with the sum of functions describing the signals and the background (dashed curve).

Thus, muon candidate tracks were selected according to the χ^2 of their track fits, qualities of their VDS–PC matches and their muon likelihoods in such a way that only about 5% of real muons were discarded. Tracks were also required to have a low probability of being a kaon according to the RICH analysis.

With these selections, the background under the J/ψ and ψ' peaks was reduced by a factor of 2.5. The signal loss due to these selections was distributed rather evenly over the kinematic range defined by Eq. (2) and was reproduced by the MC. After the selection, $(89.4 \pm 0.2)\%$ of the events in the J/ψ peak survived in the data and $(89.1 \pm 0.1)\%$ in the MC.

The dimuon mass spectra for both J/ψ and ψ' were described as a sum of two functions [22]: 1) a symmetric function, being a superposition of three Gaussians, which takes into account track resolution and effects of Molière scattering, 2) a function representing a radiative tail due to the emission of a photon in the final state of the dimuon decay $J/\psi(\psi') \rightarrow \mu^+\mu^-\gamma$.

The presence of the radiative tails and tails from Molière scattering in the invariant mass distribution of the J/ψ and ψ' signals demanded that both peaks be fit simultaneously. The total number of events in a peak was obtained by an integration of the fitted function over the full range of possible dimuon masses. The mass of the ψ' was obtained by scaling the fitted J/ψ mass by the factor $M_0(\psi')/M_0(J/\psi)$, where the M_0 were the nominal values of the respective masses. The fitted J/ψ mass resolution was rescaled for the ψ' using the dependence of the momentum resolution for the HERA-B spectrometer. The background was described as an exponent of a quadratic polynomial of the dimuon mass.

The functions describe the dimuon mass spectra well as shown in Fig.1, where $\chi^2 = 154$ for 153 degrees of freedom. The fitted mass of J/ψ is 3093 MeV/c^2 and the mass resolution (FWHM / 2.35) is 38 MeV/c^2.

5.2 Selection of J/ψ, $\psi' \rightarrow e^+e^-$

In the dielectron channel, the background was larger than for muons mainly due to misidentification of charged pions interacting in the ECAL and overlaps between energy deposits from photons and charged hadrons. Despite the higher background a careful study of the electron identification cuts resulted in J/ψ and ψ' signals of comparable purity and significance.

The first step of the event selection consisted of the requirement that track momenta lie between 4 and 400 GeV/c, corresponding to the expected range for J/ψ and ψ' decay products. Finally, an additional cut on the transverse energy of the ECAL cluster ($E_T > 1.15$ GeV) was applied in order to equalize different cut thresholds used at the pretrigger level during the acquisition periods. The signal selection was improved by rejecting electron/positron pairs having a distance of closest approach between the two tracks greater than 320 μm.

The reconstructed momentum vectors of electrons and positrons were corrected for energy lost due to bremsstrahlung (BR) emission in the material before the magnet (evaluated as about 18% on average). BR was identified and determined for each track by looking for an energy deposition in coincidence with the extrapolation of the track's VDS segment to the ECAL. The recovered energy was then added to the momentum measured by the tracking system. Being a clear signature of electrons, BR emission was also exploited to obtain a substantial background reduction, essential for an accurate counting of the small ψ' signal. It was therefore required that at least one lepton of the decaying J/ψ or ψ' had an associated BR cluster (defined as an ECAL cluster close enough to the VDS segment extrapolation).
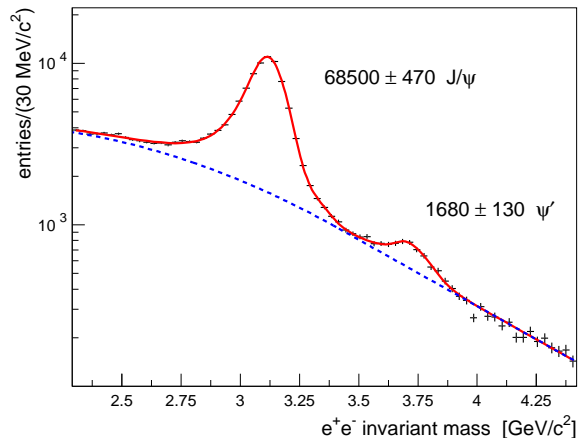
Figure 2. The invariant mass distribution of e^+e^- in the region of the J/ψ and ψ' peaks for selected dielectrons from all three materials, fitted with the sum of the functions describing the signals and the background (dashed curve).

Two additional types of selection cuts were applied to those electrons and positrons which had no associated BR cluster. The first of these cuts is on the E/p ratio, where E is the energy of the electron/positron cluster and p is the associated track momentum. The E/p distribution for electrons has a Gaussian shape with mean value close to 1 and width, $\sigma_{E/p}$, varying between 6.4% and 7.4% depending on calorimeter section. Values of E/p far from 1 correspond to particles, mostly hadrons, which release only part of their energy in the calorimeter. The second cut was applied to the distance between the reconstructed cluster and the track position extrapolated to the ECAL (Δ_x and Δ_y for the x and y direction). The Δ_x and Δ_y distributions for electrons are, apart from a small tail, well described by Gaussians centered at zero, with widths between 0.2 cm and 1.0 cm, depending on calorimeter section. A cut on these quantities leads to a significant reduction of the contamination from hadrons and random cluster-track matches, for which the $\Delta_{x(y)}$ distributions are expected to be significantly wider compared to those of the electrons.

All the above requirements were simultaneously optimized by maximizing the significance of the ψ' MC signal. The accepted ranges for E/p, Δ_x and Δ_y were respectively determined as $-1.0 \cdot \sigma_{E/p} < E/p - 1 < 3.2 \cdot \sigma_{E/p}$, $|\Delta x| < 1.7\,\sigma_x$ and $|\Delta y| < 1.8\,\sigma_y$. As a result, the S/B ratio, evaluated for the J/ψ (the only one of the two charmonium states visible also before the selection cuts), increased by about a factor of 10 with respect to the triggered events, with an efficiency for signal selection of $(34 \pm 3)\%$ in the real data and $(35.1 \pm 0.4)\%$ in the MC simulation.

To count the number of J/ψ and ψ', a Gaussian for the right part of the peak and a Breit-Wigner for the left part were used, allowing for a sizeable asymmetry of the signal due to the not fully reconstructed BR emission and a contribution from $J/\psi \to e^+e^-\gamma$ decay. Both the width and the asymmetry of the ψ' signal were kept at a fixed ratio (determined from the MC) with respect to those of the J/ψ. The background was parametrized as a Gaussian for the low invariant mass values and an exponential at higher mass, requiring continuity of the resulting function and its first derivative. The invariant mass distribution plotted in Fig. 2 shows our final selection of 68500 ± 470 J/ψ and 1680 ± 130 ψ': the resulting mass and width (of the Gaussian) of the J/ψ are, respectively, 3110 and 72 MeV/c^2. The χ^2 of the fit is 89 for 69 degrees of freedom.

6 Angular dependence of $R_{\psi'}$

Measurements of polarization (the commonly used term to denote spin alignment) provide one of the most significant tests of models of charmonia production [23]. Understanding polarization at moderate and low p_T is also important since most of the published p_T-integrated data come from the lower p_T region. The polarization of charmonium is measured by observation of the angular distribution in its decay into l^+l^-:

$$\frac{d\sigma}{d\cos\theta} \propto (1 + \lambda \cos^2\theta), \tag{4}$$

where θ is the polar angle of the l^+ with respect to the z axis of a polarization frame defined in the rest system of the charmonium state. In general, the parameter λ depends on the definition of the polarization frame [23]. The commonly used polarization frames are specified by the choice of the z axis. The three-momentum of the beam particle, $\boldsymbol{p_b}$, and that of the target, $\boldsymbol{p_t}$, in the rest system of the charmonium can be used to define the z axis.

In the Gottfried-Jackson frame, the z axis is parallel to $\boldsymbol{p_b}$, in the s-channel helicity (or recoil) frame, the z axis is defined as the direction of the charmonium three-momentum in the hadronic center-of-mass frame, i.e. it is parallel to $-(\boldsymbol{p_b} + \boldsymbol{p_t})$, and in the Collins-Soper frame, the z axis bisects the angle between $\boldsymbol{p_b}$ and $-\boldsymbol{p_t}$.

For J/ψ production, several measurements of polarization have been published. The parameter λ measured in pBe collisions [24] in the Gottfried-Jackson frame is $\lambda = 0.01 \pm 0.12 \pm 0.09$ and $\lambda = -0.11 \pm 0.12 \pm 0.09$ at 530 GeV and 800 GeV, respectively. A high statistics measurement [25, 26] in 800 GeV pCu interactions (Collins-Soper frame) resulted in $\lambda = 0.069 \pm 0.004 \pm 0.08$. The quoted errors are statistical and systematic. A measurement [27] for ψ' was performed for π^-W interactions at 253 GeV where $\lambda' = 0.02 \pm 0.14$ was obtained in the Gottfried-Jackson frame. All results are consistent with a small difference in the ψ' and J/ψ polarization. The collider result [28] (s-channel helicity frame) $\lambda' = -0.08 \pm 0.63 \pm 0.02$ for a mean p_T equal to 6.2 GeV/c is also consistent with that, but statistically less significant and, because of the relatively high p_T, not directly comparable with the fixed-target results.

In the kinematic domain (2) of HERA-B, the ψ' signal is clearly visible in the limited interval $|\cos\theta| < 0.6(0.8)$ for electrons (muons) in the Gottfried-Jackson frame. In the s-channel helicity frame the acceptance is more uniform as a function of $\cos\theta$ and $R_{\psi'}$ is measurable over the full
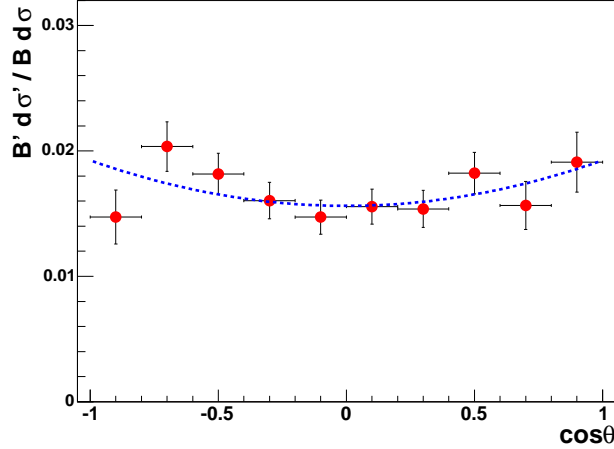
Figure 3. $R_{\psi'}$ as a function of $\cos\theta$ in the s-channel helicity frame. The dashed curve is the fitted function (5) for $\lambda = 0$ and the fitted parameter $\lambda' = 0.23 \pm 0.17$.

Table 1. The ratio of ψ' and J/ψ cross sections in the muon, $R_{\psi'}(\mu)$, electron, $R_{\psi'}(e)$, channels and for both channels combined, $R_{\psi'}$, obtained for different $\cos\theta$ intervals using the data from all targets. The value θ is the polar angle of the positive lepton in the s-channel helicity frame. Additional systematic uncertainties of 5% for the electron channel and 3% for both the muon channel and for the combined result (see Table 2) are not included here.

$\cos\theta$	$R_{\psi'}(\mu)$	$R_{\psi'}(e)$	$R_{\psi'}$
$-1.0 \div -0.8$	0.0148 ± 0.0024	0.0144 ± 0.0054	0.0147 ± 0.0022
$-0.8 \div -0.6$	0.0211 ± 0.0022	0.0169 ± 0.0046	0.0203 ± 0.0020
$-0.6 \div -0.4$	0.0203 ± 0.0019	0.0107 ± 0.0034	0.0180 ± 0.0017
$-0.4 \div -0.2$	0.0154 ± 0.0016	0.0185 ± 0.0033	0.0160 ± 0.0014
$-0.2 \div 0.0$	0.0152 ± 0.0016	0.0130 ± 0.0028	0.0147 ± 0.0014
$0.0 \div 0.2$	0.0161 ± 0.0016	0.0140 ± 0.0028	0.0156 ± 0.0014
$0.2 \div 0.4$	0.0152 ± 0.0017	0.0159 ± 0.0030	0.0154 ± 0.0015
$0.4 \div 0.6$	0.0187 ± 0.0019	0.0167 ± 0.0035	0.0182 ± 0.0017
$0.6 \div 0.8$	0.0157 ± 0.0021	0.0154 ± 0.0043	0.0156 ± 0.0019
$0.8 \div 1.0$	0.0176 ± 0.0026	0.0269 ± 0.0060	0.0191 ± 0.0024

interval of $\cos\theta$. We therefore prefer to present our results in the s-channel helicity frame. The values of $R_{\psi'}$ for ten $\cos\theta$ bins are shown in Table 1.

The dependence of $R_{\psi'}$ on $\cos\theta$ can be described as

$$\frac{B' \; d\sigma'/d\cos\theta}{B \; d\sigma/d\cos\theta} \propto \frac{1 \; + \; \lambda' \cos^2\theta}{1 \; + \; \lambda \cos^2\theta}, \tag{5}$$

where λ' and λ are related to the polarization of the ψ' and the J/ψ, respectively. The fit of $R_{\psi'}$ (see Fig. 3) with this function, where λ' is a free parameter and λ fixed, depends on the λ value, but the difference $\lambda' - \lambda$ is nearly constant. We obtain in the s-channel helicity frame

$$\Delta\lambda = \lambda' - \lambda = 0.23 \pm 0.17, \tag{6}$$

for the fit with $\lambda = 0$. To check the stability of the result, we varied λ in the interval $(-0.2, 0.2)$, which is broader than the limits given by the published measurements of J/ψ polarization, and obtained a variation of $\Delta\lambda$ in the range ± 0.04, which is much smaller than the statistical uncertainty.

7 Systematic errors of $R_{\psi'}$

The correction of the raw ψ'/ψ ratio in (1) using the efficiency ratio, ϵ/ϵ', calculated by MC was the subject of a detailed study. The efficiency ratio, ϵ/ϵ', was mainly determined by geometric factors since effects such as detector and trigger efficiencies nearly cancel out in the ratio. The geometrical factors can be calculated reliably with MC and were found to be quite stable. This is confirmed by the data since the raw ψ'/ψ ratio is also quite stable for different periods of data taking and target configurations.

Nevertheless, a small systematic bias can appear due to uncertainties in the simulation of kinematical distributions of charmonia production as well as of the detector and trigger. Possible biases were evaluated by varying parameters of the MC simulation.

The MC simulation assumed unpolarized production for J/ψ and ψ'. However, due to the limited acceptance, the efficiency ratio ϵ/ϵ' in Eq. (1) could depend on a difference between the simulated decay angular distributions for the ψ' and J/ψ. The ratio ϵ/ϵ' depends slightly, almost linearly on the difference $\lambda' - \lambda$ and consequently

$$\frac{\Delta R_{\psi'}}{R_{\psi'}} = 0.2 \, \cdot \, \Delta\lambda. \tag{7}$$

To obtain Eq. 7, we evaluated the efficiency ratio ϵ/ϵ' by simulating ψ' and J/ψ production for different $\Delta\lambda$ values in the Gottfried-Jackson frame. In this frame, the acceptance is less uniform as a function of $\cos\theta$, and the bias of $R_{\psi'}$ due to the possible difference of angular distributions for the ψ' and J/ψ is dominated by the size of $\Delta\lambda$. Theoretical arguments suggest that the difference in the ψ' and J/ψ polarization is small. The color evaporation model (CEM) predicts that λ and λ' are equal [29]. In the Nonrelativistic QCD (NRQCD) approach, the polarization of the J/ψ is larger than that of the ψ' due to feeddown from the χ_c, but λ is unlikely to exceed λ' by more than 0.2 [23]. For the HERA-B experiment, the values for λ calculated in the NRQCD approach [29] range from 0 to 0.1. We estimated the contribution to the relative systematic error due to polarization $\sigma_{sys}(R_{\psi'})/R_{\psi'} = 0.02$, corresponding to $\Delta\lambda = 0.1$ in (7).

Theoretical predictions for J/ψ and ψ' polarization in fixed-target experiments are largely independent of the target and beam types and vary slowly with beam energy [29]. Therefore direct comparison of results of different experiments is meaningful. Combining measurements [24,25,30] for λ, [27] for λ' and the HERA-B result (6), we obtained $\Delta\lambda = 0.09 \pm 0.11$. The latter estimate disfavors also a big difference between λ and λ'.

Table 2. Estimated relative systematic errors of the $R_{\psi'}$ in the $\mu^+\mu^-$, $R_{\psi'}(\mu)$, and e^+e^-, $R_{\psi'}(e)$, channels from various sources, as listed. The total uncertainty was obtained by quadratic summation.

Source of uncertainty	$\sigma_{\text{sys}}(R_{\psi'})/R_{\psi'}(\mu)$	$\sigma_{\text{sys}}(R_{\psi'})/R_{\psi'}(e)$
Polarization	0.02	0.02
p_T distribution	0.0006	0.0006
x_F distribution	0.004	0.004
Trigger simulation	0.006	0.02
Counting method	0.014	0.035
Total	0.03	0.05

To estimate the importance of the MC model used for the production kinematics, the parameters of the generated x_F and p_T distributions were changed within variations allowed by the measured differences between ψ' and J/ψ kinematics [19,31,32]. The corresponding variations of $R_{\psi'}$ were found to be rather small as listed in Table 2. Contributions to the systematic error due

to differences of kinematical distributions and polarization of ψ' and J/ψ were highly correlated for muons and electrons.

Uncertainties connected to the trigger were evaluated by removing the trigger simulation for both muons and electrons and, as a second test, increasing the value of the E_T threshold with respect to the one used by the pretrigger for electrons. These are quite extreme tests which surely overestimate possible trigger biases, nonetheless, as seen in Table 2, the changes in the $R_{\psi'}$ do not exceed 1% and 2%, for muons and electrons, respectively. Moreover, it has been verified for electrons that any systematic bias due to the BR request on the value of $R_{\psi'}$ is negligible.

The last item listed in Table 2 is related to different methods of counting the numbers of J/ψ and ψ' in (1). We obtained these values either by taking all events in the kinematic domain (2) or by summing the events in the bins of the x_F, p_T or $\cos\theta$ distributions. In doing so, the efficiencies were evaluated either for the whole kinematic domain or for the different bins.

The total relative systematic error on $R_{\psi'}$ was estimated to be 3% and 5% for the muon and electron modes, respectively. The larger error for the electron mode can be attributed to the higher contribution of background.

8 x_F and p_T dependence of $R_{\psi'}$

To obtain the ratio of the ψ' to J/ψ production cross sections times the dilepton branching ratio, $R_{\psi'}$, as a function of x_F we selected dilepton pairs in eight x_F intervals and performed the full analysis for each interval independently. The results are listed in Table 3, separately for $\mu^+\mu^-$, e^+e^- channels as well as for the combined result. Fig. 4 displays the HERA-B results together
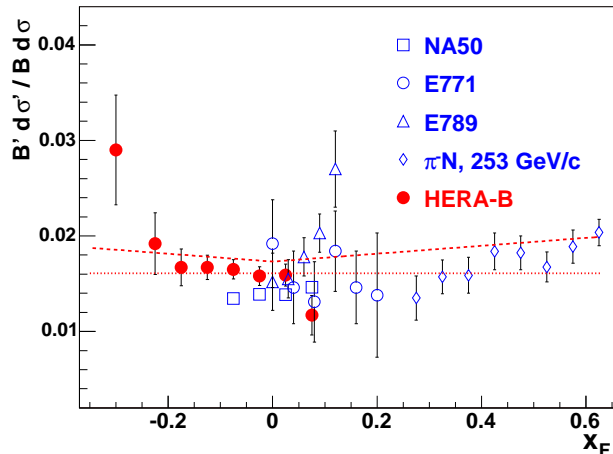
Figure 4. Measurements of $R_{\psi'}$ as a function of x_F. Results of this work, combined for μ and e decay modes and for all targets, are shown together with previous experiments which measured charmonia production in pN (NA50 [33], E771 [31], E789 [34]) and π^-N interactions [27]. Only statistical errors are shown. Two calculations, one using the NRQCD approach [36] and the other using the CEM model [35], are indicated by the dashed and dotted curves, respectively. Both calculations were made for pp interactions and corrected for the nuclear suppression in the HERA-B target as described in the text.

with earlier measurements. Neither the HERA-B nor the NA50 data [33] exhibit significant x_F dependencies. $R_{\psi'}$ measurements of E771 [31] in pN interactions extend up to $x_F = 0.2$, but suffer from large statistical errors. A statistically more accurate measurement, but performed in π^-N interactions [27], also indicates only a slow variation of $R_{\psi'}$ in the range of low and
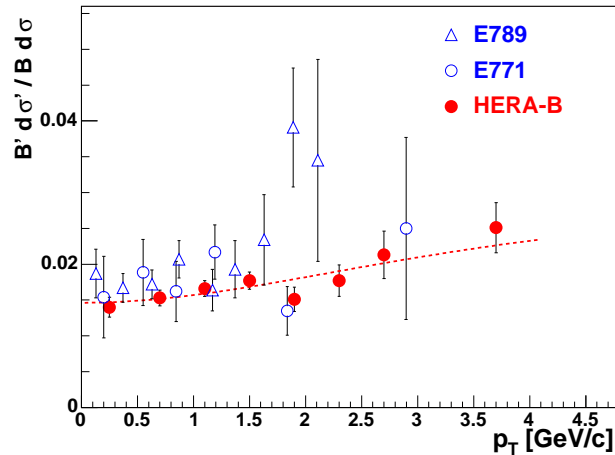
Table 3. The ratio of ψ' and J/ψ cross sections in the muon, $R_{\psi'}(\mu)$, electron, $R_{\psi'}(e)$, channels and for both channels combined, $R_{\psi'}$, obtained for intervals in x_F using the data from all targets. Additional systematic uncertainties of 5% for the electron channel and 3% for both the muon channel and for the combined result (see Table 2) are not included here.

x_F	$R_{\psi'}(\mu)$	$R_{\psi'}(e)$	$R_{\psi'}$
$-0.35 \div -0.25$	0.0309 ± 0.0076	0.0265 ± 0.0088	0.0290 ± 0.0058
$-0.25 \div -0.20$	0.0172 ± 0.0038	0.0244 ± 0.0061	0.0192 ± 0.0032
$-0.20 \div -0.15$	0.0156 ± 0.0022	0.0202 ± 0.0040	0.0167 ± 0.0019
$-0.15 \div -0.10$	0.0165 ± 0.0014	0.0175 ± 0.0030	0.0167 ± 0.0013
$-0.10 \div -0.05$	0.0162 ± 0.0011	0.0179 ± 0.0025	0.0165 ± 0.0010
$-0.05 \div \;\;\; 0.00$	0.0160 ± 0.0011	0.0152 ± 0.0022	0.0158 ± 0.0010
$0.00 \div \;\;\; 0.05$	0.0162 ± 0.0013	0.0147 ± 0.0025	0.0159 ± 0.0012
$0.05 \div \;\;\; 0.10$	0.0095 ± 0.0025	0.0165 ± 0.0037	0.0117 ± 0.0021

moderate x_F values. We may expect a similarity of the x_F behavior of the $R_{\psi'}$ in pN and π^-N interactions, because of the dominance of gluon fusion in the charmonium production process.

In the CEM [1] the differential and integrated charmonium production rates for different charmonium states should be proportional to each other and independent of projectile, target and energy. The results of the CEM for pp interactions [35] show a flat x_F behavior and agree with our results (Fig. 4). The NRQCD calculation [36] of ψ' and J/ψ production in pp interactions at 920 GeV shows a slow variation of $R_{\psi'}$ versus x_F and is consistent with our measurements as well. The results of the NRQCD and CEM models were both corrected for nuclear suppression as will be discussed in Sect. 11.

The results for $R_{\psi'}$ for eight bins in transverse momentum are given in Table 4. $R_{\psi'}$ shows a tendency to increase as a function of p_T as seen in Fig. 5. The fit of $R_{\psi'}$ with the ratio of functions of the form given in Eq. (3), where the average transverse momentum, $\langle p_T \rangle'$, for ψ' is a free parameter and $\langle p_T \rangle$ for J/ψ is fixed to the value (3), gives $\langle p_T \rangle' - \langle p_T \rangle = (0.08 \pm 0.03)\,\text{GeV}/c$. These results are consistent with those of E771 [31] and E789 [34], although the large statistical errors of these two previous measurements do not allow for a decisive test.

Figure 5. Measurements of $R_{\psi'}$ as a function of the transverse momentum. Combined results for e and μ modes obtained for all three targets are shown together with previous results from experiments E771 [31] and E789 [34]. Only statistical errors are shown. A fit of the HERA-B results with the ratio of functions (3) as described in the text, is shown by the dashed line.

Table 4. The ratio of ψ' and J/ψ cross sections in the muon, $R_{\psi'}(\mu)$, electron, $R_{\psi'}(e)$, channels and for both channels combined, $R_{\psi'}$, obtained for intervals in p_T using the data from all targets. Additional systematic uncertainties of 5% for the electron channel and 3% for both the muon channel and for the combined result (see Table 2) are not included here.

p_T [GeV/c]	$R_{\psi'}(\mu)$	$R_{\psi'}(e)$	$R_{\psi'}$
$0.0 \div 0.5$	0.0143 ± 0.0015	0.0129 ± 0.0031	0.0140 ± 0.0014
$0.5 \div 0.9$	0.0156 ± 0.0012	0.0145 ± 0.0022	0.0153 ± 0.0011
$0.9 \div 1.3$	0.0167 ± 0.0012	0.0159 ± 0.0025	0.0166 ± 0.0011
$1.3 \div 1.7$	0.0171 ± 0.0014	0.0201 ± 0.0027	0.0177 ± 0.0012
$1.7 \div 2.1$	0.0156 ± 0.0019	0.0134 ± 0.0034	0.0151 ± 0.0017
$2.1 \div 2.5$	0.0192 ± 0.0027	0.0145 ± 0.0040	0.0177 ± 0.0022
$2.5 \div 2.9$	0.0248 ± 0.0041	0.0150 ± 0.0055	0.0213 ± 0.0033
$2.9 \div 4.5$	0.0277 ± 0.0043	0.0198 ± 0.0061	0.0251 ± 0.0035

9 Combined results for $R_{\psi'}$ and for the double ratio of leptonic branching fractions

An independent analysis was performed for each target sample (C, Ti, W) and separately for both dimuon and dielectron trigger modes. For each sample the dilepton invariant mass spectra were fitted to obtain the raw ψ'/ψ ratio which was then corrected according to (1) by the efficiency ratio ϵ/ϵ'.

The values of $R_{\psi'}$ in both dilepton channels obtained for all three targets are shown in Table 5. For each target the values of $R_{\psi'}$ for the muon and electron mode were combined and the ratio $R_{\psi'}(\mu)/R_{\psi'}(e)$ was evaluated.

Table 5. The ratio of ψ' and J/ψ production cross sections per nucleus in the muon, $R_{\psi'}(\mu)$, electron, $R_{\psi'}(e)$, channels and for both channels combined, $R_{\psi'}$, for each target. The ratio $R_{\psi'}(\mu)/R_{\psi'}(e)$ is also presented. The quoted errors indicate the statistical and systematic errors, respectively.

Target	$R_{\psi'}(\mu)$	$R_{\psi'}(e)$	$R_{\psi'}$	$R_{\psi'}(\mu)/R_{\psi'}(e)$
C	$0.0166 \pm 0.0007 \pm 0.0004$	$0.0154 \pm 0.0012 \pm 0.0007$	$0.0163 \pm 0.0006 \pm 0.0005$	$1.08 \pm 0.10 \pm 0.04$
Ti	$0.0198 \pm 0.0029 \pm 0.0005$	$0.0200 \pm 0.0045 \pm 0.0009$	$0.0199 \pm 0.0024 \pm 0.0006$	$0.99 \pm 0.27 \pm 0.04$
W	$0.0158 \pm 0.0011 \pm 0.0004$	$0.0182 \pm 0.0025 \pm 0.0012$	$0.0162 \pm 0.0010 \pm 0.0005$	$0.87 \pm 0.13 \pm 0.03$

We obtained the ratio $R_{\psi'}(\mu)/R_{\psi'}(e)$, combined for all targets, as a weighted average of the three corresponding values from Table 5:

$$R_{\psi'}(\mu)/R_{\psi'}(e) = 1.00 \pm 0.08 \pm 0.04. \tag{8}$$

The quoted errors are statistical and systematic. The systematic error was estimated by comparing the results of different counting methods and by taking into account the uncertainty of trigger simulation (mainly due to the electron mode) as discussed in Sect. 7. Contributions to the systematic error due to differences of kinematical distributions and polarization of ψ' and J/ψ almost cancel out in (8).

The ratio (8) also represents a direct measurement for the double ratio of the branching fractions of the ψ' and J/ψ dilepton decays:

$$\frac{R_{\psi'}(\mu)}{R_{\psi'}(e)} = \frac{B'(\mu) \cdot B(e)}{B(\mu) \cdot B'(e)}. \tag{9}$$

The PDG values of branching ratios are [5]: $B(\mu) = (5.88 \pm 0.10)\%$, $B(e) = (5.93 \pm 0.10)\%$ for J/ψ dilepton decays and $B'(\mu) = (0.73 \pm 0.08)\%$, $B'(e) = (0.741 \pm 0.028)\%$ for ψ' decays. The
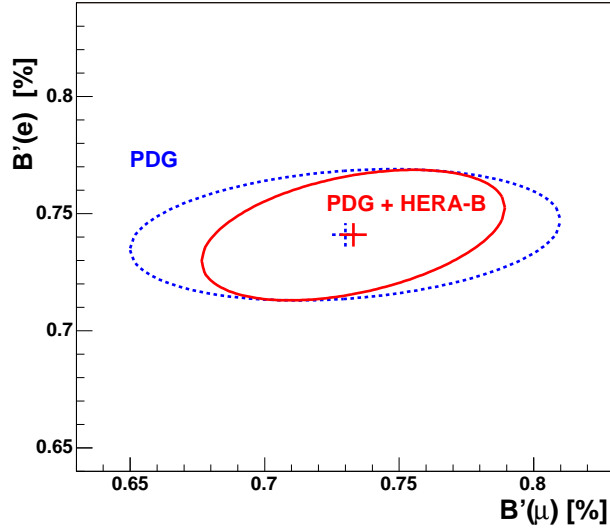
Figure 6. The error ellipse for $B'(e)$ versus $B'(\mu)$, evaluated by using the covariance matrix from [5] (dashed curve) and after (solid curve) applying the HERA-B constraint given by (8).

ψ' branching ratios are not independent since they are obtained by a global fit performed by the PDG [5], which results in $B'(\mu)/B'(e) = 0.99 \pm 0.13$. The latter value and the J/ψ branching ratios correspond to the following determination of the double ratio:

$$\frac{B'(\mu) \cdot B(e)}{B(\mu) \cdot B'(e)} \; = \; 1.00 \pm 0.13, \tag{10}$$

which is compatible with (8), but slightly less precise.

Our result (8) for $R_{\psi'}(\mu)/R_{\psi'}(e)$ would give a significant contribution as an additional constraint of the global fit of ψ' branching ratios as shown in Fig. 6. The error ellipse for $B'(e)$ versus $B'(\mu)$, evaluated by using the covariance matrix from [5], is shrunk along the $B'(\mu)$ axis (partially at the expense of a tilt, i.e. a correlation) after applying the additional HERA-B constraint by (8).

10 The x_F dependence of nuclear suppression

Usually the nuclear dependence of cross sections is parameterized as a power law with exponent α
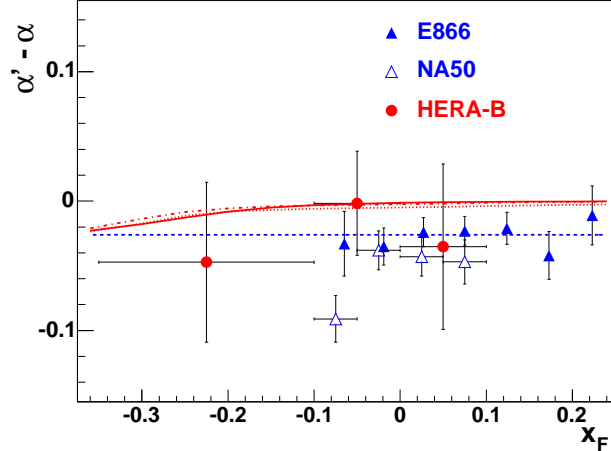
$$\sigma_A \; \propto \; A^{\alpha}, \tag{11}$$

where A is the atomic mass number. The nuclear dependence of $R_{\psi'}$ is then also a power law in A:

$$\frac{B' \sigma'_A}{B \sigma_A} \; \propto \; A^{\alpha' - \alpha} \tag{12}$$

with the parameters α' and α for the ψ' and J/ψ, respectively. Recent high statistics measurements of the nuclear dependence of J/ψ and ψ' production for proton-nucleus collisions were made at Fermilab E866 [37] and at CERN NA50 [33]. Both results are presented in terms of

$$\Delta \alpha = \alpha' - \alpha$$

Figure 7. The difference of α for ψ' and J/ψ production as a function of x_F determined from C and W data (circles), compared to results of E866 [37] (solid triangles) and NA50 [33] (triangles). A fit of the E866 results by a constant (13) is shown by the dashed line. The results of CEM for color singlet nuclear absorption [38] at 920 GeV are displayed by the solid line. The NRQCD results [38] at 450 GeV and 920 GeV are shown by the dotted and dashed-dotted curves, respectively.

for various x_F slices in Fig 7. The two results are in reasonable agreement. The HERA-B results for $\Delta\alpha$, derived from C and W data and also shown in Fig 7, are consistent with both measurements, but less accurate. The measurements shown in Fig. 7 indicate little or no x_F dependence of $\Delta\alpha$.

The calculations of nuclear suppression by the CEM for color singlet absorption and NRQCD models [38] also indicate slow x_F and collision energy dependences of $\Delta\alpha$ and that α is larger than α', however the predicted difference between α' and α is less than the measured difference. The CEM, with the additional assumptions in [39], predicts that $\Delta\alpha$ should be zero over the x_F range of this measurement. Because of the small variation of $\Delta\alpha$ in our kinematic range (2), we will use the experimental value averaged over x_F (see Sect. 11) for the analysis of our results and for comparison with calculations performed for pp interactions.

The E866 results, in the x_F range shown in Fig. 7, were fitted by a constant value:

$$\Delta\alpha(\text{E866}) \;=\; -0.026 \pm 0.005, \tag{13}$$

which will be used as an independent measurement of $\Delta\alpha$ in the analysis of $R_{\psi'}$ results in the next Sect.

11 Comparison with previous measurements

A compilation of measurements of $R_{\psi'}$ is shown in Fig. 8 (see also Table 6) together with the HERA-B results for the three targets. Previous measurements of $R_{\psi'}$ for atomic mass numbers $A > 2$ were fitted by the function

$$\frac{B'\,\sigma_A(\psi')}{B\,\sigma_A(J/\psi)} \;=\; R_{1\psi'} \cdot A^{\Delta\alpha}, \tag{14}$$

with two parameters, where $R_{1\psi'}$ is the value of the fit function when formally extrapolated to $A = 1$ and $\Delta\alpha$ is the power. The E866 value (13) was used as an additional measurement of the power in the fit. The fitted parameters are:

$$R_{1\psi'} \;=\; 0.0184 \pm 0.0004, \quad \Delta\alpha \;=\; -0.030 \pm 0.004. \tag{15}$$

Measurements performed with hydrogen and deuterium targets do not follow this simple power law dependence, as seen in Fig. 8, where the NA51 measurements [45] for pp and pd interactions are also displayed. The HERA-B results are in good agreement with the fit of previous measurements.
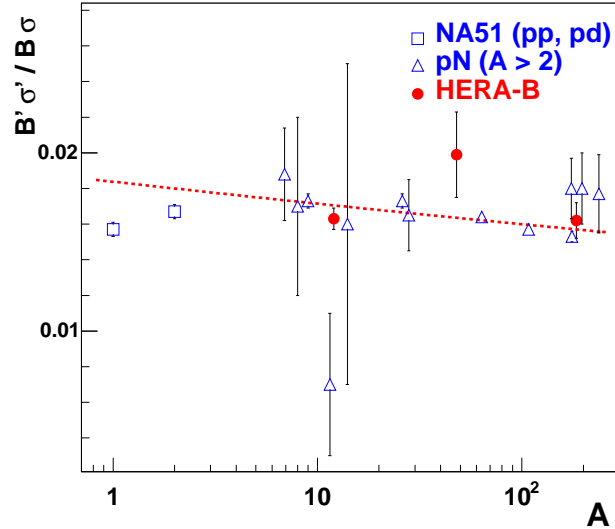
Figure 8. A compilation of measurements of $R_{\psi'}$ as a function of the atomic mass number of the target, A. All previous measurements (Table 6) for $A > 2$ (i.e. excluding NA51) are fitted (dashed line) by the function (14) with the E866 value (13) used as an additional measurement of the power in the fit. The HERA-B results combined for e and μ are also displayed.

Table 6. Ratio of ψ' and J/ψ cross sections in the dilepton channel measured in previous experiments of charmonium production by protons with momentum, p, interacting with targets with the indicated atomic mass number, A. The center–of–mass energy of the interacting nucleons, $\sqrt{s}$, is also given. The results of NA50 are listed for the "high intensity" samples since they are better suited to study the $R_{\psi'}$ ratio [33]. The measurements were performed in the dimuon channel, with the exception of the ISR experiment (last row) which detected e^+e^- pairs.

pN	A	$p(\text{GeV}/c)$	$\sqrt{s}(\text{GeV})$	$B'\sigma'/B\sigma$	Experiment
pp	1	450	29.1	$0.0157 \pm 0.0004 \pm 0.0002$	NA51 [45]
pd	2	450	29.1	$0.0167 \pm 0.0004 \pm 0.00025$	NA51 [45]
$p\text{Be}$	9	450	29.1	$0.0173 \pm 0.0004 \pm 0.0002$	NA50 [33]
$p\text{Al}$	27	450	29.1	$0.0173 \pm 0.0003 \pm 0.0004$	NA50 [33]
$p\text{Cu}$	64	450	29.1	$0.0164 \pm 0.0002 \pm 0.0002$	NA50 [33]
$p\text{Ag}$	108	450	29.1	$0.0157 \pm 0.0002 \pm 0.0002$	NA50 [33]
$p\text{W}$	184	450	29.1	$0.0153 \pm 0.0003 \pm 0.0002$	NA50 [33]
$p\text{W}$	184	200	19.4	0.0180 ± 0.0017	NA38 in [46]
$p\text{U}$	238	200	19.4	0.0177 ± 0.0022	NA38 in [46]
$p\text{Be}$	9	400	27.4	0.017 ± 0.005	E288 [47]
$p\text{C}$	12	225	20.6	0.007 ± 0.004	E331 [48]
$p\text{C}$	12	225	20.6	0.016 ± 0.009	E444 [49]
$p\text{Li}$	7	300	23.8	$0.0188 \pm 0.0026 \pm 0.0005$	E705 [32]
$p\text{Si}$	28	800	38.8	0.0165 ± 0.0020	E771 [31]
$p\text{Au}$	197	800	38.8	$0.018 \pm 0.001 \pm 0.002$	E789 [34]
pp	1	–	62.4	0.019 ± 0.007	ISR [6]

The HERA-B measurements of $R_{\psi'}$ for three targets are well fitted by the function (14) with the value $\Delta\alpha$ from (15) used as an additional measurement in the fit, resulting in

$$R_{1\psi'} = 0.0180 \pm 0.0006 \pm 0.0005,$$
$$\Delta\alpha = -0.029 \pm 0.004. \tag{16}$$

The latter $R_{1\psi'}$ value is in agreement with (15). A joint fit of previous ($A > 2$) and HERA-B
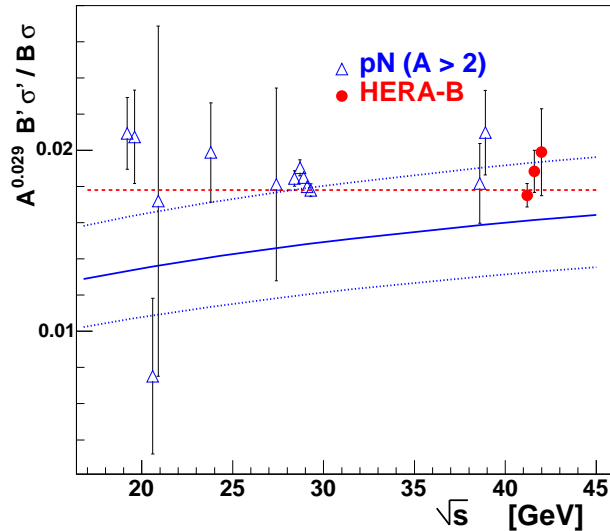
Figure 9. A compilation of measurements of $R_{\psi'}$ in the dilepton decay mode as a function of the center–of–mass energy. The measured ratios are rescaled by $A^{0.029}$ to compensate the nuclear suppression for targets with differing atomic mass number A (see Eq. (16)). The HERA-B results combined for e and μ are shown separately for C, Ti and W. The previous measurements from Table 6 (with atomic mass number, $A > 2$) are presented. The CEM expectation [35] is displayed by the dashed line. The NRQCD calculation [50] is shown by the solid line. The uncertainty of the calculation is shown by dotted lines.

measurements, using the value $\Delta\alpha$ from (13) as an additional measurement in the fit, results in $R_{1\psi'} = 0.0183 \pm 0.0003$ and $\Delta\alpha$ as given in (16).

A compilation of measurements of $R_{\psi'}$ as a function of center–of–mass energy is shown in Fig. 9. The measurements were performed with various targets and therefore need to be adjusted to compensate for nuclear effects. We assume the A-dependence given by Eq. (14) with $\Delta\alpha$ from (16) and therefore rescale all measurements by $A^{0.029}$ neglecting the error in $\Delta\alpha$. The rescaled $R_{\psi'}$ measurements are consistent with a flat energy dependence, in agreement with the CEM [35]. NRQCD calculations for $R_{\psi'}$ [50] show a slow increase with center–off-mass energy. Due to the uncertainties of the calculation such a variation of $R_{\psi'}$ is not excluded, but is disfavored.

12 Conclusions

We have performed a study of ψ' decays into $\mu^+\mu^-$ and e^+e^- using a sample of dilepton triggered data recorded during the HERA-B 2002–2003 running period. The sample was divided roughly equally between the dimuon and dielectron decay modes. The analysis was based on the selection of dilepton events with relatively low background contamination and fitting of the dilepton invariant mass spectra in the area around the J/ψ and ψ' signals. The fitted ratio of the numbers

of events in the ψ' and J/ψ peaks was corrected for the $J/\psi(\psi')$ efficiency, $\epsilon(\epsilon')$, to obtain the ratio of the ψ' and J/ψ production cross sections in the dilepton channel, $R_{\psi'}$.

For the analysis, we selected the kinematic domain (2), in which the ψ' signal was clearly visible. The efficiency ratio, ϵ/ϵ', was mainly determined by geometric factors and, therefore, was stable during the running time and reliable for MC calculations. The HERA-B results are the first measurement of $R_{\psi'}$ in the negative x_F range. The measured $R_{\psi'}$ shows little or no x_F dependence and is consistent with the previous measurements for positive x_F and with CEM and NRQCD calculations. The results suggest a slow increase of $R_{\psi'}$ with increasing p_T, although a flat p_T dependence cannot be excluded.

From the analysis of the angular dependence of $R_{\psi'}$, the difference of the polarization parameters λ for the ψ' and the J/ψ has been derived:

$$\Delta\lambda = \lambda' - \lambda = 0.23 \pm 0.17.$$

The ratios of ψ' and J/ψ production cross sections in the dilepton channel combined for the μ and e modes and measured for carbon, titanium and tungsten targets are:

$$
\begin{aligned}
B'\,\sigma'\,/\,B\,\sigma\ \text{(C)} &= 0.0163 \pm 0.0006 \pm 0.0005, \\
B'\,\sigma'\,/\,B\,\sigma\ \text{(Ti)} &= 0.0199 \pm 0.0024 \pm 0.0006, \\
B'\,\sigma'\,/\,B\,\sigma\ \text{(W)} &= 0.0162 \pm 0.0010 \pm 0.0005,
\end{aligned}
\tag{17}
$$

respectively. The quoted errors are statistical and systematic.

Assuming a nuclear dependence in the form of a power law, $R_{1\psi'} \cdot A^{\Delta\alpha}$, and using as a constraint the value $\Delta\alpha = -0.030 \pm 0.004$ obtained from previous measurements, a fit to the above values yielded:

$$R_{1\psi'} = 0.0180 \pm 0.0006 \pm 0.0005.$$

With a joint fit to HERA-B results and previous measurements for different targets ($A > 2$), assuming a power law dependence on the target atomic mass number and using the value $\Delta\alpha$ extracted from E866 results as an additional measurement in the fit, we obtained the following values for the fitted parameter:

$$R_{1\psi'} = 0.0183 \pm 0.0003, \quad \Delta\alpha = -0.029 \pm 0.004.$$

The HERA-B results (17) indicate no significant energy dependence of $R_{\psi'}$ with respect to previous measurements at lower energies.

Averaging over all three targets yields the ratio:

$$R_{\psi'}(\mu)/R_{\psi'}(e) = 1.00 \pm 0.08 \pm 0.04$$

This result confirms $e - \mu$ universality in dilepton decays of the ψ' with an accuracy which is better than can be achieved using only current PDG branching ratios for the ψ' and J/ψ dilepton decays. The result can be used as an additional constraint to update the PDG branching ratios for ψ' dilepton decays.

13 Acknowledgments

References

1. H. Fritzsch, Phys. Lett. **B67** (1977) 217.
2. R. Baier and R. Rückl, Phys. Lett. **B102** (1981) 364; Z. Phys. **C19** (1983) 251.
3. E. L. Berger, D. L. Jones, Phys. Rev. **D23** (1981) 1521.
4. G. T. Bodwin, E. Braaten and G. P. Lepage, Phys. Rev. **D51** (1995) 1125; erratum *ibid.* **D55** (1997) 5853.
5. S. Eidelman et al., Review of Particle Physics, Phys. Lett. **B 592** (2004) 1 and 2005 partial update for edition 2006.
6. A.G. Clark et al., Nucl. Phys. **B 142** (1978) 29.
7. T. Lohse et al. (HERA-B Collaboration), DESY–PRC–94–02 (1994).
8. E. Hartouni et al., *HERA-B Design Report*, DESY–PRC–95–01 (1995).
9. K. Ehret et al., Nucl. Instr. Meth. **A 446** (2000) 190.
10. C. Bauer et al., Nucl. Instr. Meth. **A 501** (2003) 39.
11. T. Zeuner et al., Nucl. Instr. Meth. **A 446** (2000) 324.
12. H. Albrecht et al., Nucl. Instr. Meth. **A 541** (2005) 610.
13. H. Albrecht et al., Nucl. Instr. Meth. **A 555** (2005) 310.
14. I. Ariño et al., Nucl. Instr. Meth. **A 453** (2000) 289.
15. A. Zoccoli et al., Nucl. Instr. Meth. **A 446** (2000) 246.
16. M. Buchler et al., IEEE Trans. on Nucl. Sci. **46** (1999) 126;
    M. Arefiev et al., IEEE Trans. on Nucl. Sci. **48** (2001) 1059.
17. T. Sjöstrand, Comp. Phys. Comm. **82** (1994) 74.
18. H. Pi, Comp. Phys. Comm. **82** (1992) 173.
19. A. Zoccoli, Proc. of the International Conference on Hard and Electromagnetic Probes of High Energy Collisions, Ericeira, Portugal, November 4–10, 2004, Eur. Phys. J. **C43** (2005) 179.
20. R. Brun et al., *GEANT3*, Internal Report CERN DD/EE/84-1, CERN (1987).
21. S. Nowak, *HBGEAN. A description of HERA-B GEANT*, HERA-B note 94-123 (1994).
22. A. Spiridonov, *Bremsstrahlung in Leptonic Onia Decays: Effects on Mass Spectra*, DESY 04-105 (2004), hep-ex/0510076.
23. M. Beneke and I.Z. Rothstein, Phys. Rev. **D 54** (1996) 2005.
24. A. Gribushin et al., Phys. Rev. **D 62** (2001) 012001.
25. T.H. Chang et al., Phys. Rev. Lett. **91** (2001) 211801.
26. T.H. Chang, Ph.D. Thesis, New Mexico State University, 1999, hep-ex/0012034.
27. J.G. Heinrich et al., Phys. Rev. **D 44** (1991) 1909.
28. T. Affolder et al. (CDF Collaboration), Phys. Rev. Lett. **85** (2000) 2886.
29. N. Brambilla et al., *Heavy Quarkonium Physics*, Published as CERN Yellow Report, CERN-2005-005 (2005), Geneva, CERN, hep-ph/0412158.
30. T. Alexopoulos et al., Phys. Rev. **D 55** (1997) 3927.
31. T. Alexopoulos et al., Phys. Lett. **B 374** (1996) 271.
32. L. Antoniazzi et al., Phys. Rev. **D 46** (1992) 4828.
33. B. Alessandro et al. (NA50 Collaboration), Eur. Phys. J. **C 33** (2004) 31.
34. M.H. Schub et al., Phys. Rev. **D 52** (1995) 1307.
35. R. Gavai et al., Int. J. Mod. Phys. **A 10** (1995) 3043.
36. R. Vogt, Phys. Rev. **C 61** (2000) 035203.
37. M.J. Leitch et al., Phys. Rev. Lett. **84** (2000) 3256.
38. R. Vogt, Nucl. Phys. **A 700** (2002) 539.
39. D. Kharzeev, H. Satz, Phys. Lett. **B 366** (1996) 316.
40. M. Beneke et al., Phys. Rev. **D 57** (1998) 4258.
41. E. Braaten et al., Phys. Rev. **D 62** (2000) 094005.
42. C. Akerlof et al., Phys. Rev. **D 48** (1993) 5067.
43. A. Gribushin et al., Phys. Rev. **D 53** (1996) 4723.
44. M.C. Abreu et al. (NA38 Collaboration), Phys. Lett. **B 466** (1999) 408.
45. M.C. Abreu et al. (NA51 Collaboration), Phys. Lett. **B 438** (1998) 35.
46. C. Lourenço, Ph.D. Thesis, Universidade Tećnica de Lisboa, 1995.
47. H.D. Snyder et al. (E288 Collaboration), Phys. Rev. Lett. **36** (1976) 1415.
48. J.G. Branson et al. (E331 Collaboration), Phys. Rev. Lett. **38** (1977) 1331.
49. K.J. Anderson et al. (E444 Collaboration), Phys. Rev. Lett. **42** (1979) 944.
50. F. Maltoni et al., Phys. Lett. **B 638** (2006) 202.